PHYSICS

Ultrafast electron diffraction from nanophotonic waveforms via dynamical Aharonov-Bohm phases

K. J. Mohler[1], D. Ehberger[1], I. Gronwald[2], C. Lange[2]*, R. Huber[2], P. Baum[1,3†]

Copyright © 2020 The Authors, some rights reserved; exclusive licensee American Association for the Advancement of Science. No claim to original U.S. Government Works. Distributed under a Creative Commons Attribution NonCommercial License 4.0 (CC BY-NC).

Electron interferometry via phase-contrast microscopy, holography, or picodiffraction can provide a direct visualization of the static electric and magnetic fields inside or around a material at subatomic precision, but understanding the electromagnetic origin of light-matter interaction requires time resolution as well. Here, we demonstrate that pump-probe electron diffraction with all-optically compressed electron pulses can capture dynamic electromagnetic potentials in a nanophotonic material with sub-light-cycle time resolution via centrosymmetry-violating Bragg spot dynamics. The origin of this effect is a sizable quantum mechanical phase shift that the electron de Broglie wave obtains from the oscillating electromagnetic potentials within less than 1 fs. Coherent electron imaging and scattering can therefore reveal the electromagnetic foundations of light-matter interaction on the level of the cycles of light.

INTRODUCTION

According to Aharonov and Bohm (*1*), two parts of a coherent electron wave packet that travel along two distinct trajectories will acquire a quantum mechanical phase shift that is directly related to the electromagnetic potentials along these trajectories. This principle has profound implications in electron microscopy, where it is ubiquitous for the description of coherent electron scattering from various types of macroscopic and atomistic electromagnetic fields (*2*–*5*). For example, electric polarization and magnetic flux in nanostructures (*2*, *3*) or the electric fields in the chemical bonds between the atoms in a crystal (*4*, *5*) have been elucidated in this way, and ponderomotive phase plates are discussed as an enabling technique for cryogenic electron microscopy and high-resolution biomolecular imaging (*6*).

However, all such electron interferometric investigations with electron holography (*2*, *3*), differential phase contrast (*2*, *3*), and atomic picodiffraction (*4*, *5*) now involve slow time scales, far from the ultrahigh frequencies in the terahertz and petahertz regimes that would be required to visualize the functionality of complex optical materials and metamaterials (*7*–*12*) on subwavelength and subcycle dimensions in space and time (*13*–*16*). While ultrafast electron microscopy and diffraction with laser-generated femtosecond electron pulses are widespread approaches for investigating structural dynamics and atomic motions in molecules and condensed matter (*17*–*21*), the resolution of ultrafast electrodynamic phenomena has, so far, only been achieved through incoherent point particle scattering (*14*, *22*) and not by any electron interferometric technique, although a time-resolved version of electron holography or diffraction with sub-light-cycle time resolution would promise a noninvasive and sensitive way to visualize optical and nanophotonic phenomena at the full versatility of modern electron microscopy and diffraction devices with their highly coherent beams.

RESULTS

Here, we report how ultrafast small-angle diffraction with time-compressed electron pulses can be used to examine the rapidly oscillating electrodynamic potentials around an optically excited nanostructure array with subcycle time resolution. The basis of our measurement concept is the conjecture that interferometric phase shifts according to Aharonov and Bohm may, with sufficiently short electron wave packets, become relevant at frequencies approaching those of light, even if the magnetic and electric contributions are rapidly oscillating and strongly interlinked. Our experiment is depicted in Fig. 1A. A two-dimensional array of metal nanostructures (black, compare Fig. 1B) on a dielectric substrate mimics a metasurface (*7*, *10*) or a field-enhancing periodic nanostructure for nonlinear optics (*11*). Illumination with a single-cycle terahertz waveform (red, compare Fig. 1C) induces rapidly changing near fields (black arrows, see Fig. 1A) and therefore oscillating electromagnetic potentials in proximity of the material. Femtosecond single-electron probe pulses (blue, compare Fig. 1D), generated via all-optical compression (*23*), produce coherent multibeam interference and therefore small-angle diffraction patterns (green) as a function of delay time. While the shape of the nanostructure itself is not altered by the excitation field, the electromagnetic potentials induced at the nanostructures by the excitation field cycles may modulate the quantum mechanical phase of the electron wave function as a function of space and time. The corresponding changes of the diffraction pattern may therefore reveal the sample's electromagnetic dynamics with nanometer and sub-light-cycle precision.

Figure 2 shows the static small-angle diffraction data of our nanostructure array as obtained with femtosecond single-electron pulses. Although the electron de Broglie wavelength of 4.3 pm at 75 keV central energy is >20,000 times smaller than the unit cell of the metal structure (82×100 nm^2), the intrinsic transverse coherence of single-electron pulses allows us to observe a two-dimensional set of Bragg spots up to fourth order. We label the Bragg spots by Miller indices (hk), where h and k are integer numbers. A third Miller index is omitted because our nanostructure is not periodic in the z direction and the reciprocal space therefore crosses the Ewald sphere at no particular Laue zone. The measured small-angle diffraction (Fig. 2A) agrees well with the theoretical pattern (Fig. 2B) derived from the measured static nanostructure (see Materials and Methods). Figure 2

[1]Ludwig-Maximilians-Universität München, Am Coulombwall 1, 85748 Garching, Germany. [2]Universität Regensburg, Universitätsstraße 31, 93053 Regensburg, Germany. [3]Universität Konstanz, Universitätsstr. 10, 78464 Konstanz, Germany.
*Present address: Fakultät Physik, Technische Universität Dortmund, Otto-Hahn-Straße 4, 44227 Dortmund, Germany.
†Corresponding author. Email: peter.baum@uni-konstanz.de

Konstanzer Online-Publikations-System (KOPS)
URL: http://nbn-resolving.de/urn:nbn:de:bsz:352-2-1vdg595xbj7xq4

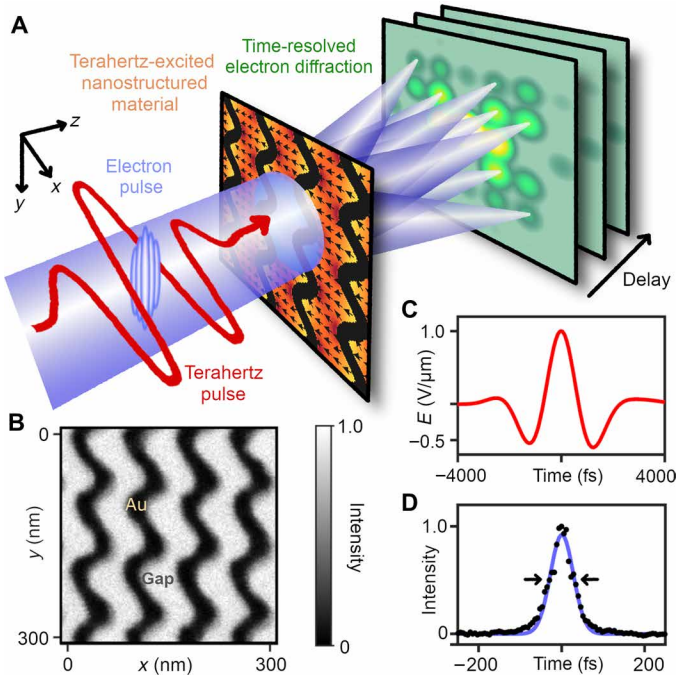

Fig. 1. Time-resolved small-angle electron diffraction from oscillating electromagnetic potentials. (**A**) Concept and experimental setup. A terahertz pulse (red) excites a photonic nanostructure (orange) and induces local electrodynamic fields (arrows). Ultrashort electron pulses (blue) are diffracted and probe the electromagnetic potentials as a function of delay time. The origin of the diffraction changes (green) are phase shifts of the electron de Broglie wave by the local electric and magnetic potentials. (**B**) Scanning electron microscopy image of the nanostructure (inverted). The size of the unit cell is 82 × 100 nm^2. (**C**) Electric field of the terahertz excitation pulse with a central frequency of 0.35 THz. (**D**) Measured temporal profile of the electron pulses (dots) with a Gaussian fit (solid). The full width at half maximum is 60 fs (black arrows).

(C to E) shows three integrated regions of the measured diffraction data (black dots) in comparison to the theoretical results (green solid line).

When turning on the single-cycle electromagnetic excitation (see Fig. 1C), we see several substantial and distinct modifications to the measured diffraction pattern as a function of the terahertz-electron time delay (see Fig. 2F). The most obvious feature is a time-dependent deflection of the whole diffraction pattern along x, the polarization direction of the terahertz field. The temporal shape of this global deflection (see Fig. 2G) is almost symmetric in time; the initial rise at −1.8 ps toward higher angular deflections is as fast as the final decay toward zero deflection at +1.8 ps. The Bragg spots remain discernible throughout the entire terahertz-electron delay range, although the maximum time-dependent global deflection exceeds the inverse lattice constant by four times. Their spacing remains constant at only minor changes of contrast and width. However, we observe substantial Bragg spot intensity changes as a function of delay. In Fig. 2 (H and I), we compare the integrated relative intensities of $(1\bar{1})$ and (11) with the average of $(\bar{1}\bar{1})$ and $(\bar{1}1)$, because these pairs share a common first Miller index and therefore project similarly to the excitation's polarization along the x axis. The maximum relative intensity changes are ±8%, and the opposing temporal shapes have maxima and minima occurring at the turning points of the global deflection (dashed lines).

In our ultrafast small-angle diffraction experiment, the incident terahertz radiation triggers a wealth of delay-dependent phenomena that are caused by purely electromagnetic effects and not by structural changes of the material. To understand the origin of these observations, we analyze the quantum mechanical phase shifts that an electron experiences when passing through time-dependent electromagnetic potentials. This approach is necessitated by the interferometric nature of our diffraction experiment with delocalized electrons beyond the point particle approximation. Along a given closed loop in space and time, the electron wave function obtains a quantum mechanical phase shift according to the line integral (*1*)

$$\phi_{AB} = \frac{e}{\hbar}\oint A_\mu \, dx^\mu \tag{1}$$

where e is the elementary charge, $\hbar$ is the reduced Planck constant, $x^\mu = (ct, x, y, z)$ is the position 4-vector, and $A_\mu = \left(\frac{\varphi}{c}, -A_x, -A_y, -A_z\right)$ is the electromagnetic 4-potential composed of the electric scalar potential φ and three components of the magnetic vector potential A_x, A_y, and A_z.

Figure 3A illustrates the necessary space-time integration of Eq. 1 in an interaction volume that evolves rapidly in time. The electrons in the nearly collimated beam of our experiment travel at constant velocity along approximately straight trajectories parallel to the z direction. We therefore assume an incoming electron wave function $\psi_i(x, y, \Delta t)$ with a flat phase front $\phi_{AB}(x, y, \Delta t) = 0$ (light blue). After passage through the relevant interaction volume (gray), the exit wave function obtains a spatially modulated phase map $\Delta\phi_{AB}(x, y, \Delta t)$ depending on its arrival time Δt with respect to the excitation field. For each delay time and lateral position, $\Delta\phi_{AB}(x, y, \Delta t)$ is calculated by the closed space-time integral around the area spanned by a path 2 along the z direction at x and y and a selected reference path 1 (see Fig. 3A). The red dashed parts are zero because there are no fields and potentials long before and long after the arrival of the excitation pulse.

For application of this framework to our experiment, we decompose the optical response of our nanostructure into far-field contributions with macroscopic dimensions and the nanophotonic near-field components that occur within the unit cells. Under long-wavelength excitation, the macroscopic far-field response of our wavy nanostructure mimics a wire grid polarizer and can be approximated as a planar beam splitter of unknown reflectivity that is exposed to a superposition of incident plane waves that the terahertz pulses are composed of. An analytical treatment via Eq. 1 of electrons passing through the incident, reflected, and transmitted electromagnetic potentials of a thin beam splitter with arbitrary splitting ratio and absorption (see Materials and Methods) reveals that any net effects from the macroscopic vector potential cancel out to zero for copropagating electrons and an excitation wave vector at normal incidence (see Fig. 1A), in accordance with previous experiments for metals or dielectrics (*24*, *25*). Therefore, the macroscopic response of the nanostructure itself cannot produce the measured changes in diffraction, i.e. the global deflection and the Bragg spot intensity changes.

On a mesoscopic length scale, smaller than a terahertz wavelength but much larger than a unit cell, there are resonances caused by the sample support structure (see Materials and Methods). Such resonances have been seen to deflect a transmitted electron beam as a function of time (*14*, *23*). To quantify the magnitude of these effects for our sample and for calibration of the incoming terahertz

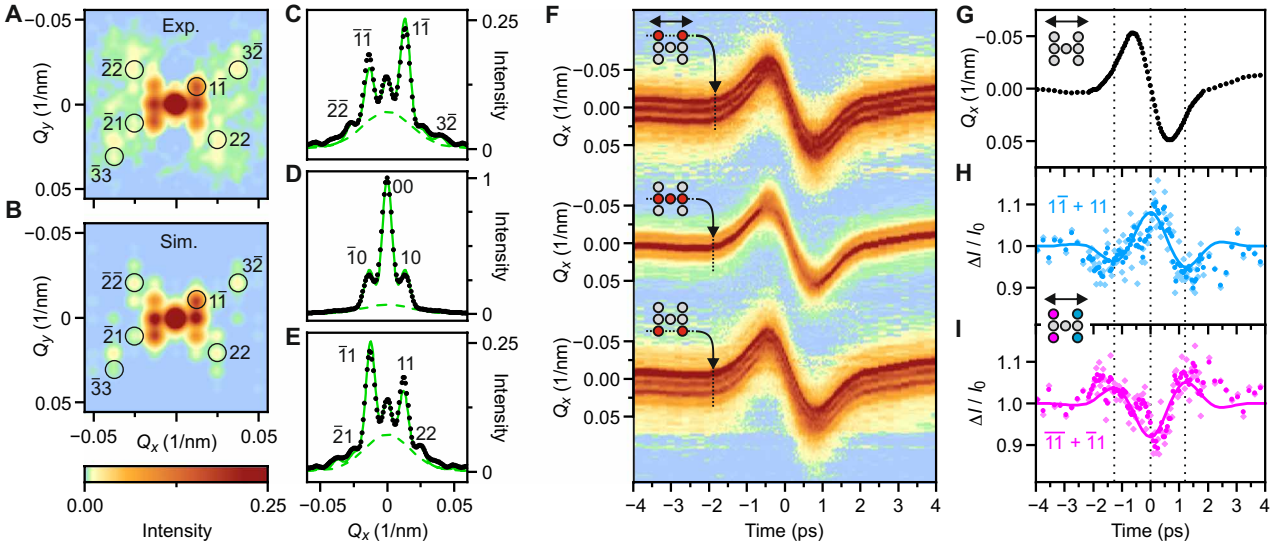

Fig. 2. Experimental ultrafast diffraction results in comparison to simulations. (**A**) Measured static small-angle diffraction after subtraction of an inelastic background (see Materials and Methods). The appearance of third-order spots in the *x* direction and fourth-order spots in the *y* direction indicates a sub-unit-cell resolution of ~25 nm in both dimensions. The different intensities of ($1\bar{1}$) and ($\bar{1}1$) compared to (11) and ($\bar{1}\bar{1}$), consistent in experiment and theory, reflect the deviations of our static wavy nanostructure from a sinusoidal pattern. (**B**) Theoretical small-angle diffraction derived from the measured scanning electron microscopy image (see Fig. 1B). (**C**) Integrated intensity (black dots) of the minus-first and minus-second order in the *y* direction in comparison to theory (green solid line). Dashed line, inelastic scattering background. (**D**) Integrated intensity (black dots) for the zeroth order in the *y* direction. (**E**) Integrated intensity (black dots) of the plus-first and plus-second order in the *y* direction. (**F**) Visualization of the three-dimensional time-dependent diffraction data in the time-Qx domain obtained from the terahertz-excited nanostructure. The top, middle, and bottom panels show the temporal evolution of the three *y*-integrated regions depicted in (C) to (E). The red dots in the insets indicate the major Bragg spots that are plotted as a function of time. The black arrow in the uppermost inset indicates the excitation polarization. The color bar is identical to (B) but with an upper limit of 0.75. (**G**) Global deflection as a function of time delay. (**H**) Relative Bragg spot intensity (blue diamonds, raw data; blue dots, smoothed) of $1\bar{1}$ and 11 in comparison to simulations (solid line) as a function of time. (**I**) Relative Bragg spot intensity of $\bar{1}\bar{1}$ and $\bar{1}1$ (magenta diamonds, raw data; magenta dots, smoothed) in comparison to the simulations (solid line). These Bragg spots project along the excitation polarization (inset, black arrow).

waveform, we measure the global deflection of three different resonant structures that are subjected to the same terahertz waveform and compare the data to simulations. The origin of these deflections are mesoscopic resonances that globally affect the entire diffraction pattern, so the coherence properties of the electron beam remain untouched and nontrivial quantum contributions beyond a classical description via Lorentz forces and point particles are not expected. The results (fig. S1) reveal the cosine-like incoming terahertz pulse shape depicted in Fig. 1C and confirm that mesoscopic resonances can fully explain the measured global deflection, including the phase shift of approximately 90° of the single-cycle Bragg pattern motion with respect to the impinging electromagnetic wave (compare Figs. 1C and 2G).

On the microscopic dimensions of the unit cell, we numerically obtain the time-dependent and structure-specific electromagnetic fields (see Fig. 3, B and C) from finite-difference time-domain simulations (see Materials and Methods). At the depicted instance in time, the electric near fields point predominantly toward negative *x* but have a periodic component along *y* that arises from the wavy nature of our nanostructure. Induced surface charges counteract the incident electric field inside the conducting material and cause a peak field enhancement by a factor of ~5 in the gap where adjacent gold rods come closest. Gold has a vanishing terahertz magnetic susceptibility, but dynamical currents almost perfectly cancel the magnetic fields inside the wavy structures. The potentials and fields in our experiment can therefore not be produced by any electrostatic and/or magnetostatic experiment, and the diffraction experiment explores a purely dynamical setting.

A characterization of the initiated sub-unit-cell dynamics and the inflicted changes to the time-resolved diffraction patterns, arising from the coherent interference of electron de Broglie waves, requires consideration of the spatiotemporal quantum phases that are imprinted on the electron wave function via the electromagnetic potentials, as described in Eq. 1. Using the numerically obtained electromagnetic fields, we apply four Poisson equations in Coulomb gauge (see Materials and Methods) to obtain the time-dependent 4-potential A_μ (Fig. 3, D and E) as a function of space and time. Inside the metal, we see a gradient of the electric potential φ that results from momentary charge separation. The corresponding electric field is cancelled by the time derivative of the magnetic vector potential A_x of the incident wave (not depicted in Fig. 3). To model the excited nanostructure's effects on the electrons, we apply a phase-object approximation. Position-dependent and delay-dependent phase shifts $\Delta\phi_{AB}(x, y, \Delta t)$ of the electron wave function are derived from the calculated potentials according to Eq. 1 and Fig. 3A, and spatially varying transmission amplitudes are taken from the measured static structure of Fig. 1B. The far-field diffraction pattern is computed via Fourier transformation.

Figure 2 (H and I) shows the simulated Bragg spot intensities (solid lines) in comparison to the measured spot intensities of the experiment (dots). The simulations reproduce the measured Bragg spots' asymmetric intensities and their evolution in synchrony to the shape of the terahertz excitation field (see Fig. 1C), thereby linking the observed violation of centrosymmetry to the excitation-induced electromagnetic potentials. Only the absolute degree of asymmetry is three to five times higher in the experiment as compared to the

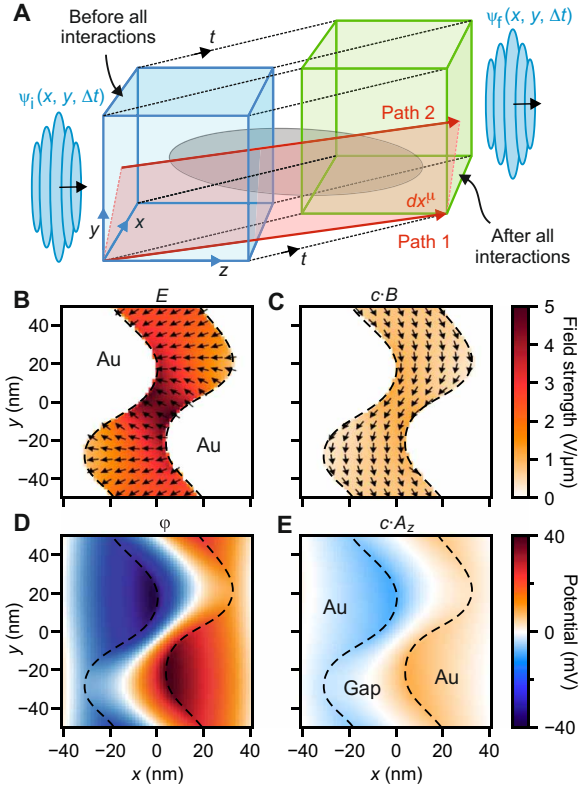

Fig. 3. Theoretical framework for ultrafast electron phase changes in diffraction. (**A**) Space-time diagram and world lines for simulating time-dependent phase maps imprinted on an incoming plane electron wave function ψ_i by interaction with a time-dependent electromagnetic potential (gray). Phase shifts are calculated as a function of lateral position and delay time via closed loops (red) according to Eq. 1. (**B**) Time-dependent electric field vectors in the example structure at $\Delta t = 0$ fs. (**C**) Magnetic field vectors. (**D**) Electric scalar potential at the example of $\Delta t = 0$ fs. (**E**) Magnetic vector potential, component along the propagation direction; all in Coulomb gauge.

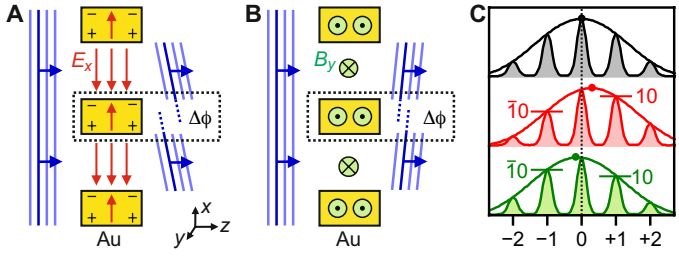

Fig. 4. One-dimensional model. (**A**) Electron de Broglie waves (blue) and electric fields E_x (red) in and around the gold rods (yellow) after subtraction of the plane wave background. The phase shifts Δϕ (blue, dotted) that are related to fields in the enclosed areas (black, dotted). (**B**) Magnetic fields B_y (green) and their weaker phase shift Δϕ with opposite sign. (**C**) Corresponding one-dimensional diffraction orders for no excitation (black), electric-only effects (red), and magnetic-only contributions (green). Dots, centers of the diffraction envelopes. Solid lines, asymmetric intensity changes of the Bragg spots.

calculations, attributed to our neglect of nonnormal wall directions, the specific refractive index of nanostructured gold, additional field enhancements from surface roughness, and uncertainties in determining our structure's thickness along *z*. The observation of delay-dependent Bragg spot intensities synchronous with the excitation-induced electromagnetic potentials demonstrates that ultrafast small-angle electron diffraction can noninvasively capture and reveal via potential-induced electron phase changes the nanophotonic response of a nanostructured material with subwavelength and subcycle precision in space and time.

DISCUSSION

A one-dimensional simplification can help elucidate some of the observed dynamics (see Fig. 4). To this end, we neglect our structure's local curvatures and approximate it as a grid of linear wires under long-wavelength, nonresonant excitation. The far field of the incoming terahertz pulse can be subtracted, because it does not affect the final diffraction pattern and, in particular, the Bragg spot intensities (see above). We obtain the electromagnetic near fields as depicted in Fig. 4 (A and B). In the gaps, the electric and magnetic fields are approximately constant and imprint linear phase shifts onto an incoming plane electron wave (blue lines). The fields enclosed by the black boxes cause additional phase jumps Δϕ between the upper and lower edges of the gold rods, so that the periodicity of the fields directly maps into periodic phase distributions. Magnetically induced phases oppose the electric ones, but our nanostructure favors electric over magnetic field enhancement, and this break in symmetry causes net Bragg spot intensity changes to appear in diffraction (see Fig. 4C). Violations of centrosymmetry in Bragg diffraction (horizontal lines) arise from delay-dependent shifts (dots) of the envelope function with respect to stationary Bragg spot positions, complying with our observations at $\Delta t = 0$ (see Fig. 2, G to I), where the measured Bragg spots locate at the original position but with asymmetric intensities. In a way, the experiment at $\Delta t = 0$ mimics the unequal diffraction intensities that can be produced by a blazed diffraction grating in optics, but here in a dynamical setting and with changes caused by purely quantum mechanical effects according to Eq. 1 rather than by shaping a physical structure.

Asymmetric Bragg spot intensities induced by the presence of electromagnetic potentials are also a key signature of conventional Aharonov-Bohm settings that aim at identifying phase shifts resulting from nonlocal electromagnetic fields (*1*, *26*). Pointing out the significance of the electromagnetic potentials for maintaining the principle of locality, Aharonov and Bohm predicted, for example, the imprint of relative phase shifts on electrons traveling along trajectories that enclose the static magnetic field of a long solenoid even without local exposure to its field. While such magnetostatic phase shifts have been confirmed by experiments (*26*, *27*), discussions are still ongoing for dynamical settings in which electric and magnetic fields are interlinked and potentials become a function of space and time (*28*–*30*). For our wavy nanostructure array, periodic phase distributions result not only from local interaction with the fields along the electron's trajectory but also from enclosed space-time regions (dashed in Fig. 4, A and B) in which fields are present that are not directly encountered by the electrons but shape the corresponding potentials. In the one-dimensional picture of Fig. 4, the measured excitation-induced asymmetry of Bragg spot intensities is caused by a shift of the diffraction pattern's envelope function over stationary Bragg spot positions (see Fig. 4C). In this regard, our terahertz-induced diffraction setting is complementary to an array of magnetic solenoids as a periodic version of the standard Aharonov-Bohm experiment. There, the electron wave obtains a ladder of phase steps (*26*) that, by shifting the Bragg spot positions underneath a

stationary envelope function (*31*), results in asymmetric intensity changes comparable to our case. The measurement of asymmetric intensity changes for our nanostructured array at frequencies approaching those of light therefore indicates that electromagnetic potentials are of equal significance in highly dynamical settings as in static ones and demonstrates that terahertz-compressed electron pulses can provide a valuable technology for studying the Aharonov-Bohm effect at 10^9 times higher frequencies than accessible before (*32*, *33*).

We touch here an extreme limit of quantum-coherent light-electron interaction, the topic of many recent reports (*34*, *35*). In contrast to studies with near-infrared light (*34*, *35*), where photon-order sidebands appear in the spectrum, the electron wave function in our experiment is much smaller than a wavelength of the radiation in free space and its temporal coherence is much smaller than a cycle period. In other words, the electrons seem like point particles with respect to the optical waveform, like in all other electron-terahertz interactions reported so far. Nevertheless, substantial quantum effects are required for explaining the interaction in our experiment. We see that the quantum nature of free electrons is present irrespectively of the wave packet dimensions if a proper setting for analysis is applied. This result will have implications for laser-driven particle accelerators, quantum optics in electron microscopy, terahertz-based beam metrology, and all other activities aiming at shaping or analyzing a free electron by the cycles of radiation.

In combination, the reported results and simulations establish a quantum mechanical picture of electron-nanostructure interaction in the presence of dynamical electromagnetic excitation fields at frequencies approaching those of light. Ultrashort electron pulses, if made shorter than half a cycle of the excitation period, probe the position-dependent and time-dependent optical near fields in nanophotonic materials via the quantum mechanical phase shifts caused by the oscillating electrodynamic potentials. This probing process is noninvasive, not entangled with the excitation and does not distort the fields and dynamics in the structure (see Materials and Methods). Attosecond transit times through near fields are sufficient for substantial and detectable electron-optical phase changes to occur, if the magnetic and electric contributions do not cancel out. Accordingly, dynamical light-matter interaction can be measured on the level of the cycles of light with the full interferometric sensitivity offered by electron holography and related techniques. The spatiotemporal resolutions of ultrafast electron interferometry and diffraction will ultimately be only limited by the picometer-scale de Broglie wavelength of beam electrons and the ability to compress them into pulses with attosecond duration (*22*, *36*, *37*). Accordingly, combining our technique with attosecond electron pulses will allow us to investigate subcycle material responses at wavelengths down to the visible and ultraviolet range of the optical spectrum. Although, in practice, the number of electrons per pulse, the transverse beam coherence, and the pulse duration are interlinked, modern ultrafast transmission electron microscopes or table-top diffraction apparatuses provide ample possibilities for optimizations according to the specific requirements for an intended investigation. The reported direct susceptibility of electron matter waves to the electromagnetic potentials of light waves therefore advances electron diffraction, holography, ptychography, and related electron interferometric imaging methods from their established stationary settings to the domain of light-matter interaction on the time scale of the optical cycles of light, to visualize and understand the functionality of nanophotonic specimen, metamaterials, or photocatalytic compounds via their electromagnetic responses in space and time.

MATERIALS AND METHODS

Nanostructure design and fabrication

A 50-nm-thick silicon nitride membrane is covered with a positive electron beam resist by spin coating. The periodic wavy pattern is written via electron beam lithography at an acceleration voltage of 30 kV. After resist development, a titanium adhesion layer with a thickness of 5 nm and a gold layer with a thickness of 25 nm are deposited by physical vapor deposition. The lift-off process is conducted in acetone. The structured area measures $120 \times 120\ \mu m^2$ with a unit cell size of $82 \times 100\ nm^2$. A solid gold frame with a size of $250 \times 250\ \mu m^2$ (see extended Fig. 1A) covers the outer, unstructured part of the window to block the electron beam outside of the nanostructures.

Generation of electron pulses and excitation fields

Ultrafast electron diffraction at highest time resolution requires high electron energies to minimize dispersion effects and the electron pulse duration (*38*), although lower electron energies would facilitate small-angle diffraction (*39*). We generate electron pulses at an energy of 75 keV via femtosecond two-photon photoemission from an optical focal spot of ~5 μm diameter (*40*). Electron beam expansion to a diameter of ~2 mm provides a transverse coherence length of ~100 nm (full width at half maximum) (*41*). The electron pulses are compressed in time with terahertz radiation (*23*) at a planar metal membrane (*38*). Streaking measurements (*23*) reveal a pulse duration of ~25 fs (root mean square) or ~60 fs (full width at half maximum) at the position of the sample (see Fig. 1D). To avoid space-charge effects, we generate only 4 ± 2 electrons per pulse at the source and less than one electron per pulse arrives at the sample. Terahertz single-cycle pulses for nanostructure excitation are obtained from laser-generated Cerenkov radiation in $LiNbO_3$ (*42*). A camera (F416, TVIPS GmbH) with a pixel size of $15.6 \times 15.6\ \mu m^2$ is used for electron detection. Sporadic broken pixels are removed by nearest-neighbor averaging. The reported time-resolved results are, to our knowledge, the first demonstration of a pump-probe diffraction experiment with terahertz-compressed electron pulses at the superior time resolution that they provide.

Compensation of magnetic stray fields

Nanodiffraction at our high electron energy of 75 keV produces very tiny diffraction angles below 0.1 mrad. The sharpness of the measured diffraction patterns is mainly limited by magnetic stray fields in the laboratory. Slow drifts are compensated by Helmholtz coils (MACOM, Müller BBM Gmbh). To compensate for magnetic field oscillations from the laboratory mains, we place electrostatic deflection plates behind the sample that split the diffraction patterns in a stepwise manner into 10 separate copies along the direction perpendicular to the terahertz-induced deflection (see Fig. 2) and in synchrony to the 50-Hz period of the laboratory voltage. With the help of Gaussian fits, we superimpose the individual images and thus produce diffraction patterns that are almost as sharp as allowed by spatial coherence of the electron beam.

Static and dynamic electron diffraction patterns

To increase the signal-to-noise ratio, the measured static diffraction data are symmetrized by harnessing the centrosymmetric characteristics of static diffraction patterns as the absolute square of the Fourier transformation of a real-valued object. For display, interpolation by a factor of 3 was performed in Fig. 2A. The theoretical

static diffraction pattern of Fig. 2B is derived by thresholding the scanning electron microscopy image of Fig. 1B and averaging over the unit cell, followed by a Fourier transformation. The electron beam is treated as an incoherent sum of coherent single-electron wave packets (*41*) that impinge with random displacements with respect to the unit cell. Comparison with the experimental data yields an estimate for the inelastic scattering background (green dashed lines in Fig. 2, C to E). Figure 2F is interpolated by a factor of 7 and Bragg spot intensities are fitted with a polynomial peak detection algorithm as products of amplitude and width, whereby width changes are determined from the correlated amplitude changes of all four evaluated spots. Data from the three regions are plotted with a displacement for comparison. In Fig. 2 (I and H), the dark blue and dark magenta dots are obtained by a three-point moving average of the raw data (blue and magenta diamonds).

Global deflection by mesoscopic resonances and characterization of the terahertz waveform

The measured global deflections originate from the support structures around the sample and characterize the electromagnetic waveform of the incoming terahertz radiation. Figure S1 shows three mesoscopic structures and their measured dynamics (black dots). Finite-difference time-domain calculations on micrometer dimensions and propagation of the electrons as point particles through the resulting electromagnetic fields produce the green lines. A global fit of the incoming terahertz waveform under variation of the central frequency, pulse duration, and carrier-envelope phase converges to the field depicted in Fig. 1C.

Finite-difference time-domain simulations of sub-unit-cell dynamics

By exploiting the collinear geometry of the experiment, for which all unit cells experience locally the same physics in space and time, the finite-difference time-domain calculations can be restricted to one single unit cell with periodic boundary conditions. For saving memory, we use a wave with a frequency of 35 THz of which the wavelength is still >100 times larger than the unit cell. In this regime, the field enhancement is wavelength independent (*43*). Gold is approximated as a perfect metal.

Calculation of the 4-potential from simulated *E* and *B* fields

Calculations of dynamical diffraction effects, originating from the electrodynamics around the nanostructure, require a quantum mechanical approach, because the electrons spread coherently over multiple unit cells. Reported methods to simulate quantum mechanical laser-electron interactions at nanostructures include analytical methods (*44*) and hybrid approaches with a Maxwell-Schrödinger framework (*45*). For our approach via Eq. 1, we need the 4-potential $A_\mu(x, y, z, t)$, but our finite-difference time-domain simulations only deliver E and B. We solve $\vec{E} = -\nabla\varphi - \frac{\partial\vec{A}}{\partial t}$ and $\vec{B} = \nabla\times\vec{A}$ for $\vec{A}$ and φ in Coulomb gauge via transformation into four Poisson equations, $\nabla\vec{E} = -\Delta\varphi - \partial(\nabla\vec{A})/\partial t = -\Delta\varphi$ and $\nabla\times\vec{B} = \nabla\cdot(\nabla\vec{A}) - \nabla^2\vec{A} = -\Delta\vec{A}$. The boundary conditions are periodic in x and y, the directions perpendicular to the direction of electron and terahertz propagation. Along z, we apply a Dirichlet condition for φ, because there are no electric charges far away from the nanostructure. For the boundary conditions of A, we harness the Stokes theorem together with a plane wave approximation far away from the nanostructure. The resulting $A(x, y, z, t)$ and $\varphi(x, y, z, t)$ in the simulation volume provide the basis for calculating delay-dependent phase maps $\phi(x, y, \Delta t)$ according to Eq. 1 and Fig. 3A.

Electromagnetic plane wave background

The macroscopic quantum mechanical effects of the terahertz far fields to the electron wave function are calculated by modeling the wavy nanostructure array as a thin beam splitter and using Eq. 1. The incoming terahertz wave is treated as a superposition of incident plane waves with polarization in the xz plane. Complex reflection and transmission coefficients $r_0e^{i\varphi_r}$ and $t_0e^{i\varphi_t}$ imprint phases (φ_r and φ_t) and amplitude changes (r_0 and t_0) on the electromagnetic radiation. The scalar potential is set to zero in Coulomb gauge. A plane wave incident at an angle α_{THz} and the resulting reflected wave are therefore given in the region $z \le 0$ by the magnetic vector potentials

$$\begin{pmatrix} A_z^{in} \\ A_x^{in} \end{pmatrix} = \begin{pmatrix} -\sin(\alpha_{THz}) \\ \cos(\alpha_{THz}) \end{pmatrix} \frac{E_0}{\omega} \cos(\omega t - k\sin(\alpha_{THz})\,x - k\cos(\alpha_{THz})\,z) \tag{2}$$

$$\begin{pmatrix} A_z^{ref} \\ A_x^{ref} \end{pmatrix} = \begin{pmatrix} -\sin(\alpha_{THz}) \\ -\cos(\alpha_{THz}) \end{pmatrix} r_0 \frac{E_0}{\omega} \cos(\omega t - k\sin(\alpha_{THz})\,x + k\cos(\alpha_{THz})\,z + \varphi_r) \tag{3}$$

The transmitted wave in the region $z > 0$ is expressed by

$$\begin{pmatrix} A_z^{trans} \\ A_x^{trans} \end{pmatrix} = \begin{pmatrix} -\sin(\alpha_{THz}) \\ \cos(\alpha_{THz}) \end{pmatrix} t_0 \frac{E_0}{\omega} \cos(\omega t - k\sin(\alpha_{THz})\,x - k\cos(\alpha_{THz})\,z + \varphi_t) \tag{4}$$

Here, t is time, ω is the angular frequency, E_0 is the electric field amplitude, and k is the wave number. The phase shift of the electron wave function is calculated by inserting Eqs. 2 to 4 into Eq. 1. For tracing electron trajectories through the oscillating electromagnetic cycles, we assume parallel paths at an incident angle α_e, constant velocity v, a time delay Δt, and spacing of $\cos(\alpha_e)\Delta x$. We let the resulting line integrals converge by assuming a slowly decreasing terahertz field strength at $\pm\infty$. With the reduced Planck constant $\hbar$, the elementary charge e, $\beta = \frac{v}{c}$, and an electron beam diameter much smaller than the terahertz wavelength, the resulting phase shifts of the electron wave function are given by

$$\Delta\phi_{AB}^{in} = \frac{eE_0}{\hbar\omega}\left[\frac{\sin(\alpha_{THz} - \alpha_e)}{(1 - \beta\cos(\alpha_{THz} - \alpha_e))}\right] \cos(\omega\Delta t)\,(\sin(\alpha_e) - \beta\sin(\alpha_{THz}))\,\Delta x \tag{5}$$

$$\Delta\phi_{AB}^{ref} = +r_0\frac{eE_0}{\hbar\omega}\left[\frac{\sin(\alpha_{THz} + \alpha_e)}{(1 + \beta\cos(\alpha_{THz} + \alpha_e))}\right] \cos(\omega\Delta t + \varphi_r)\,(\sin(\alpha_e) - \beta\sin(\alpha_{THz}))\,\Delta x \tag{6}$$

$$\Delta\phi_{AB}^{trans} = -t_0\frac{eE_0}{\hbar\omega}\left[\frac{\sin(\alpha_{THz} - \alpha_e)}{(1 - \beta\cos(\alpha_{THz} - \alpha_e))}\right] \cos(\omega\Delta t + \varphi_t)\,(\sin(\alpha_e) - \beta\sin(\alpha_{THz}))\,\Delta x \tag{7}$$

for the incident, reflected, and transmitted wave. In general, these phase shifts are linear functions of Δx and can therefore lead to

global beam deflections, as seen in experiments with metals or dielectrics (*24*, *25*, *46*). However, for the experiment's collinear geometry at normal incidence ($\alpha_e = \alpha_{THz} = 0$), all phase shifts and the corresponding global deflections vanish independently of Δt and the beam splitting properties of the structure.

Noninvasive probing

Excitation is made with a freely propagating electromagnetic pump pulse that impinges onto the sample without distortions. A probing electron passes through the nanostructures' near field within a time $t_{trans} < 0.3$ fs and experiences an electric near field of $E < 5 \times 10^6$ V/m. The highest energy ΔW that the electron can possibly exchange with potential longitudinal field components is $\Delta W \approx eEt_{trans}\nu < 0.2$ eV, which is about 10^{12} times smaller than the terahertz pulse energy of 15 nJ that is applied for sample excitation.

SUPPLEMENTARY MATERIALS

Supplementary material for this article is available at http://advances.sciencemag.org/cgi/content/full/6/47/eabc8804/DC1

REFERENCES AND NOTES

1. Y. Aharonov, D. Bohm, Significance of electromagnetic potentials in the quantum theory. *Phys. Rev.* **115**, 485–491 (1959).
2. H. Lichte, P. Formanek, A. Lenk, M. Linck, C. Matzeck, M. Lehmann, P. Simon, Electron holography: Applications to materials questions. *Annu. Rev. Mater. Res.* **37**, 539–588 (2007).
3. M. R. McCartney, D. J. Smith, Electron holography: Phase imaging with nanometer resolution. *Annu. Rev. Mater. Res.* **37**, 729–767 (2007).
4. K. Müller, F. F. Krause, A. Béché, M. Schowalter, V. Galioit, S. Löffler, J. Verbeeck, J. Zweck, P. Schattschneider, A. Rosenauer, Atomic electric fields revealed by a quantum mechanical approach to electron picodiffraction. *Nat. Commun.* **5**, 5653 (2014).
5. W. Gao, C. Addiego, H. Wang, X. X. Yan, Y. S. Hou, D. X. Ji, C. Heikes, Y. Zhang, L. Z. Li, H. X. Huyan, T. Blum, T. Aoki, Y. F. Nie, D. G. Schlom, R. Wu, X. Pan, Real-space charge-density imaging with sub-angstrom resolution by four-dimensional electron microscopy. *Nature* **575**, 480–484 (2019).
6. O. Schwartz, J. J. Axelrod, S. L. Campbell, C. Turnbaugh, R. M. Glaeser, H. Müller, Laser phase plate for transmission electron microscopy. *Nat. Methods* **16**, 1016–1020 (2019).
7. A. V. Kildishev, A. Boltasseva, V. M. Shalaev, Planar photonics with metasurfaces. *Science* **339**, 1232009 (2013).
8. X. J. Ni, Z. J. Wong, M. Mrejen, Y. Wang, X. Zhang, An ultrathin invisibility skin cloak for visible light. *Science* **349**, 1310–1314 (2015).
9. E. Maguid, I. Yulevich, D. Veksler, V. Kleiner, M. L. Brongersma, E. Hasman, Photonic spin-controlled multifunctional shared-aperture antenna array. *Science* **352**, 1202–1206 (2016).
10. M. Khorasaninejad, F. Capasso, Metalenses: Versatile multifunctional photonic components. *Science* **358**, eaam8100 (2017).
11. M. Sivis, M. Taucer, G. Vampa, K. Johnston, A. Staudte, A. Y. Naumov, D. M. Villeneuve, C. Ropers, P. B. Corkum, Tailored semiconductors for high-harmonic optoelectronics. *Science* **357**, 303–306 (2017).
12. G. H. Yuan, N. I. Zheludev, Detecting nanometric displacements with optical ruler metrology. *Science* **364**, 771–775 (2019).
13. M. Eisele, T. L. Cocker, M. A. Huber, M. Plankl, L. Viti, D. Ercolani, L. Sorba, M. S. Vitiello, R. Hober, Ultrafast multi-terahertz nano-spectroscopy with sub-cycle temporal resolution. *Nat. Photonics* **8**, 841–845 (2014).
14. A. Ryabov, P. Baum, Electron microscopy of electromagnetic waveforms. *Science* **353**, 374–377 (2016).
15. T. L. Cocker, D. Peller, P. Yu, J. Repp, R. Huber, Tracking the ultrafast motion of a single molecule by femtosecond orbital imaging. *Nature* **539**, 263–267 (2016).
16. A. Polman, M. Kociak, F. J. García de Abajo, Electron-beam spectroscopy for nanophotonics. *Nat. Mater.* **18**, 1158–1171 (2019).
17. H. Ihee, V. A. Lobastov, U. M. Gomez, B. M. Goodson, R. Srinivasan, C. Y. Ruan, A. H. Zewail, Direct imaging of transient molecular structures with ultrafast diffraction. *Science* **291**, 458–462 (2001).
18. R. J. D. Miller, Femtosecond crystallography with ultrabright electrons and x-rays: Capturing chemistry in action. *Science* **343**, 1108–1116 (2014).
19. B. J. Siwick, J. R. Dwyer, R. E. Jordan, R. J. D. Miller, An atomic-level view of melting using femtosecond electron diffraction. *Science* **302**, 1382–1385 (2003).
20. P. Baum, D. S. Yang, A. H. Zewail, 4D visualization of transitional structures in phase transformations by electron diffraction. *Science* **318**, 788–792 (2007).
21. T. Frigge, B. Hafke, T. Witte, B. Krenzer, C. Streubühr, A. Samad Syed, V. M. Trontl, I. Avigo, P. Zhou, M. Ligges, D. von der Linde, U. Bovensiepen, M. Horn-von Hoegen, S. Wippermann, A. Lücke, U. Gerstmann, W. G. Schmidt, Optically excited structural transition in atomic wires on surfaces at the quantum limit. *Nature* **544**, 207–211 (2017).
22. Y. Morimoto, P. Baum, Diffraction and microscopy with attosecond electron pulse trains. *Nat. Phys.* **14**, 252–256 (2018).
23. C. Kealhofer, W. Schneider, D. Ehberger, A. Ryabov, F. Krausz, P. Baum, All-optical control and metrology of electron pulses. *Science* **352**, 429–433 (2016).
24. D. Ehberger, A. Ryabov, P. Baum, Tilted electron pulses. *Phys. Rev. Lett.* **121**, 094801 (2018).
25. Y. Morimoto, P. Baum, Attosecond control of electron beams at dielectric and absorbing membranes. *Phys. Rev. A* **97**, 033815 (2018).
26. M. Becker, G. Guzzinati, A. Beche, J. Verbeeck, H. Batelaan, Asymmetry and non-dispersivity in the Aharonov-Bohm effect. *Nat. Commun.* **10**, 1700 (2019).
27. A. Tonomura, N. Osakabe, T. Matsuda, T. Kawasaki, J. Endo, S. Yano, H. Yamada, Evidence for Aharonov-Bohm effect with magnetic field completely shielded from electron wave. *Phys. Rev. Lett.* **56**, 792–795 (1986).
28. B. Barwick, H. Batelaan, Aharonov-Bohm phase shifts induced by laser pulses. *New J. Phys.* **10**, 083036 (2008).
29. D. Singleton, E. C. Vagenas, The covariant, time-dependent Aharonov-Bohm effect. *Phys. Lett. B* **723**, 241–244 (2013).
30. S. R. Choudhury, S. Mahajan, Direct calculation of time varying Aharonov-Bohm effect. *Phys. Lett. A* **383**, 2467–2471 (2019).
31. G. Pozzi, C. B. Boothroyd, A. H. Tavabi, E. Yücelen, R. E. Dunin-Borkowski, S. Frabboni, G. C. Gazzadi, Experimental realization of the Ehrenberg-Siday thought experiment. *Appl. Phys. Lett.* **108**, 083108 (2016).
32. L. Marton, J. A. Simpson, J. A. Suddeth, An electron interferometer. *Rev. Sci. Instrum.* **25**, 1099–1104 (1954).
33. F. G. Werner, D. R. Brill, Significance of electromagnetic potentials in the quantum theory in the interpretation of electron interferometer fringe observations. *Phys. Rev. Lett.* **4**, 344–347 (1960).
34. O. Kfir, H. Lourenço-Martins, G. Storeck, M. Sivis, T. R. Harvey, T. J. Kippenberg, A. Feist, C. Ropers, Controlling free electrons with optical whispering-gallery modes. *Nature* **582**, 46–49 (2020).
35. K. Wang, R. Dahan, M. Shentcis, Y. Kauffmann, A. Ben Hayun, O. Reinhardt, S. Tsesses, I. Kaminer, Coherent interaction between free electrons and a photonic cavity. *Nature* **582**, 50–54 (2020).
36. K. E. Priebe, C. Rathje, S. V. Yalunin, T. Hohage, A. Feist, S. Schäfer, C. Ropers, Attosecond electron pulse trains and quantum state reconstruction in ultrafast transmission electron microscopy. *Nat. Photonics* **11**, 793–797 (2017).
37. M. Kozák, N. Schönenberger, P. Hommelhoff, Ponderomotive generation and detection of attosecond free-electron pulse trains. *Phys. Rev. Lett.* **120**, 103203 (2018).
38. D. Ehberger, K. J. Mohler, T. Vasileiadis, R. Ernstorfer, L. Waldecker, P. Baum, Terahertz compression of electron pulses at a planar mirror membrane. *Phys. Rev. Appl.* **11**, 024034 (2019).
39. B. McMorran, J. D. Perreault, T. Savas, A. Cronin, Diffraction of 0.5 keV electrons from free-standing transmission gratings. *Ultramicroscopy* **106**, 356–364 (2006).
40. L. Kasmi, D. Kreier, M. Bradler, E. Riedle, P. Baum, Femtosecond single-electron pulses generated by two-photon photoemission close to the work function. *New J. Phys.* **17**, 033008 (2015).
41. F. O. Kirchner, A. Gliserin, F. Krausz, P. Baum, Laser streaking of free electrons at 25 keV. *Nat. Photonics* **8**, 52–57 (2014).
42. M. V. Tsarev, D. Ehberger, P. Baum, High-average-power, intense THz pulses from a LiNbO3 slab with silicon output coupler. *Appl. Phys. B Lasers Opt.* **122**, 30 (2016).
43. A. Novitsky, A. M. Ivinskaya, M. Zalkovskij, R. Malureanu, P. Uhd Jepsen, A. V. Lavrinenko, Non-resonant terahertz field enhancement in periodically arranged nanoslits. *J. Appl. Phys.* **112**, 074318 (2012).
44. I. Madan, G. M. Vanacore, E. Pomarico, G. Berruto, R. J. Lamb, D. McGrouther, T. T. A. Lummen, T. Latychevskaia, F. J. García de Abajo, F. Carbone, Holographic imaging of electromagnetic fields via electron-light quantum interference. *Sci. Adv.* **5**, eaav8358 (2019).
45. N. Talebi, Schrödinger electrons interacting with optical gratings: Quantum mechanical study of the inverse Smith-Purcell effect. *New J. Phys.* **18**, 123006 (2016).
46. G. M. Vanacore, I. Madan, G. Berruto, K. Wang, E. Pomarico, R. J. Lamb, D. McGrouther, I. Kaminer, B. Barwick, F. J. García de Abajo, F. Carbone, Attosecond coherent control of free-electron wave functions using semi-infinite light fields. *Nat. Commun.* **9**, 2694 (2018).

Acknowledgments: We acknowledge preliminary experiments by A. Gliserin and thank F. Krausz for generous support and laboratory infrastructure. **Funding:** This work was supported by the European Research Council (CoG no. 647771) and the Munich-Centre for Advanced Photonics (MAP). Financial support from the Deutsche Forschungsgemeinschaft (DFG) through CRC 1277, grant no. 314695032 (subproject A05), is gratefully acknowledged.
Author contributions: P.B. conceived the experiment. K.J.M. performed the experiments with D.E.'s assistance. K.J.M. analyzed the data. K.J.M. and P.B. devised the theory, and K.J.M. performed the numerical calculations. I.G., C.L., and R.H. designed, produced, and characterized the wavy nanostructures. P.B. and K.J.M. wrote the paper with input from all authors. **Competing interests:** The authors declare that they have no competing interests. **Data and materials availability:** All data needed to evaluate the conclusions in the paper are present in the paper and/or the Supplementary Materials. Additional data related to this paper may be requested from the authors.

Submitted 19 May 2020
Accepted 8 October 2020
Published 20 November 2020
10.1126/sciadv.abc8804

Citation: K. J. Mohler, D. Ehberger, I. Gronwald, C. Lange, R. Huber, P. Baum, Ultrafast electron diffraction from nanophotonic waveforms via dynamical Aharonov-Bohm phases. *Sci. Adv.* **6**, eabc8804 (2020).

Science Advances

Ultrafast electron diffraction from nanophotonic waveforms via dynamical Aharonov-Bohm phases

K. J. Mohler, D. Ehberger, I. Gronwald, C. Lange, R. Huber and P. Baum

Sci Adv **6** (47), eabc8804.
DOI: 10.1126/sciadv.abc8804

ARTICLE TOOLS http://advances.sciencemag.org/content/6/47/eabc8804

SUPPLEMENTARY MATERIALS http://advances.sciencemag.org/content/suppl/2020/11/16/6.47.eabc8804.DC1

REFERENCES This article cites 46 articles, 13 of which you can access for free
http://advances.sciencemag.org/content/6/47/eabc8804#BIBL

PERMISSIONS http://www.sciencemag.org/help/reprints-and-permissions

Use of this article is subject to the Terms of Service

Science Advances (ISSN 2375-2548) is published by the American Association for the Advancement of Science, 1200 New York Avenue NW, Washington, DC 20005. The title *Science Advances* is a registered trademark of AAAS.

Copyright © 2020 The Authors, some rights reserved; exclusive licensee American Association for the Advancement of Science. No claim to original U.S. Government Works. Distributed under a Creative Commons Attribution NonCommercial License 4.0 (CC BY-NC).